

Genus-0 Surface Parameterization using Spherical Beltrami Differentials*

Zhehao Xu[†] and Lok Ming Lui[‡]

Abstract.

Spherical surface parameterization is a fundamental tool in geometry processing and imaging science. For a genus-0 closed surface, many efficient algorithms can map the surface to the sphere; consequently, a broad class of task-driven genus-0 mapping problems can be reduced to constructing a high-quality spherical self-map. However, existing approaches often face a trade-off between satisfying task objectives (e.g., landmark or feature alignment), maintaining bijectivity, and controlling geometric distortion. We introduce the Spherical Beltrami Differential (SBD), a two-chart representation of quasiconformal self-maps of the sphere, and establish its correspondence with spherical homeomorphisms up to conformal automorphisms. Building on the Spectral Beltrami Network (SBN) [31], we propose a neural optimization framework BOOST that optimizes two Beltrami fields on hemispherical stereographic charts and enforces global consistency through explicit seam-aware constraints. Experiments on large-deformation landmark matching and intensity-based spherical registration demonstrate the effectiveness of our proposed framework. We further apply the method to brain cortical surface registration, aligning sulcal landmarks and jointly matching cortical sulci depth maps, showing improved task fidelity with controlled distortion and robust bijective behavior.

Key words. surface mesh, quasiconformal mapping, surface parametrization, deep learning

AMS subject classifications. 65D18, 65K10, 68T07,

1. Introduction. Diffeomorphic mappings are key in computational geometry and medical imaging for surface registration and shape analysis, preserving topology and geometry. Mathematically, a mapping $f : \mathcal{M} \rightarrow \mathcal{N}$ between Riemannian manifolds \mathcal{M} and \mathcal{N} is diffeomorphic if it is a bijection with a smooth inverse. Among all practices, the 3D genus-0 closed surface mapping problem gains attention due to its relevance in the real world, as well as the lack of accurate and generic methods. For example, brain surface registration enables standardized comparisons between individuals for statistical analysis [25]. Over the past decades, numerous works have been proposed to solve this problem. In terms of data form, they can be divided into two main classes, surface mesh [4, 5, 12, 28] and point cloud [3, 16, 32, 33].

By the uniformization theorem, the problem of optimizing a mapping from a genus-0 closed surface to another one is equivalent to finding an optimized mapping from the sphere to itself, satisfying certain properties. Established numerical tools [4, 6, 9], provide conformal spherical parameterizations, ensuring angle preservation. However, a conformal sphere parameterization is usually not desired. For example, some focus on area preserving [2, 27] and some are interested in finding parameterizations best aligning features [1, 11]. Our research objective is to provide a generic and accurate algorithm for this **diffeomorphic spherical parameterization problem**, formulated mathematically as finding an optimal sphere self-mapping such that

$$(1.1) \quad f = \operatorname{argmin}_{g: \mathbb{S}^2 \rightarrow \mathbb{S}^2} E(g) \text{ subject to } g \in \mathcal{C},$$

*Submitted to the editors DATE.

Funding: The second author was supported by HKRGC GRF (Project ID: 14307621).

[†]Department of Mathematics, The Chinese University of Hong Kong (zhxu@math.cuhk.edu.hk).

[‡]Department of Mathematics, The Chinese University of Hong Kong (lmliu@math.cuhk.edu.hk).

where E is the energy functional by which the solution would satisfy desired properties, and \mathcal{C} is the constraint space in which two factors are indispensable: bijectivity and geometric regularity. For example, in the landmark constrained conformal mapping problem [18, 24], to get a bijective and plausible deformation, it is necessary to control the local geometric distortion like angle distortion. Across real-life applications, simultaneous satisfaction of feature alignment, bijectivity, and bounded geometric distortion is crucial but difficult. High-fidelity feature matching tends to introduce severe local stretching while enforcing diffeomorphism and controlled geometric distortion counteracts this tendency. Balancing these terms yields a highly nonconvex landscape with many spurious minima.

Existing methods can be broadly categorized into two groups. The first group optimizes vertex positions directly on the 3D surface. These approaches, which include techniques like Ricci flow [14] and harmonic energy minimization [17], are intuitive but suffer from two major drawbacks: the optimization landscape is highly non-convex, and there is no inherent guarantee of bijectivity, sometimes leading to self-intersections. The second group performs optimization on a planar domain [2, 4, 13, 15], typically the complex plane \mathbb{C} , after an initial stereographic projection. While this simplifies the optimization in some respects, it also faces some issues. For example, boundary constraints are needed because it is a single-chart spherical parameterizations while the unit sphere cannot be covered by a single chart. Additionally, it might induce significant distortion that occurs around the pole of the projection.

A diffeomorphism can be characterized not only by where each vertex moves but also by how the map locally shears and stretches. Considering this, it is natural to explore representing a diffeomorphism by quantities measuring geometric distortion. For a Riemann surface, the Beltrami differential $\mu = \{\mu_\alpha\}$ lives in the complex tangent bundle and measures conformal distortion. To overcome limitations of traditional work, we propose representing the self-diffeomorphism of S^2 by **spherical Beltrami differential**, a streamlined variant tailored to the sphere. Given this differential, we recover the map via the **Least-Squares Quasiconformal (LSQC) energy** [29]. Moreover, numerical implementation of LSQC enjoys properties like existence and uniqueness of minimizer, correspondence with homeomorphisms, invariant by similarity transformation, and independent of resolution of the mesh. However, differentiating through the classical LSQC solver is computationally prohibitive. To overcome this, in the previous work [31] we introduce **Spectral Beltrami Network (SBN)**, a deep neural network designed to act as a differentiable surrogate for the LSQC solver.

To solve the diffeomorphic spherical parameterization problem, we propose a novel algorithm, **Beltrami Optimization On Spherical Topology (BOOST)**. BOOST represents a spherical map using two stereographic charts (hemispheres), optimizes the corresponding Beltrami fields using the SBN. The spherical Beltrami differential formalism provides the mathematical object these two fields represent: a single global spherical quasiconformal map once cross-chart compatibility is satisfied. In practice, BOOST enforces this compatibility through seam boundary matching, folding penalties after stitching, and seam smoothness regularization. This two-chart formulation avoids the pole distortions inherent in single-chart spherical parameterizations and enables flexible, distortion-controlled diffeomorphic registration on genus-0 surfaces, with applications to cortical surface alignment and hybrid landmark/feature matching.

The organization of the paper is as follows. In Sec.2, previous related works are reviewed.

and contributions are mentioned in Sec.3. In Sec.4, some of the related mathematical concepts are introduced. In Sec.5, we propose the concept spherical Beltrami differential and show its correspondence with spherical quasiconformal mappings, and introduce the model Spectral Beltrami Network. In Sec.6, We establish the neural optimization framework BOOST. In Sec.8, multiple experiments are conducted to show the capability and potential of our work in complex imaging problems. In Sec.9, we analyze the key factors hidden behind the excellence of the model and briefly discuss its limitations as well as potential future work. In Sec.10, a conclusion is given.

2. Previous works. The spherical parameterization problem of genus-0 closed surfaces has been widely studied, with methods broadly categorized into optimization on the spherical surface and optimization on the parameterization domain.

Gu and Yau in [10] proposed a nonlinear gradient descent algorithm to compute global spherical conformal parameterizations for genus-0 surfaces, which is done in the tangent spaces of the sphere, but often converges slowly and cannot guarantee bijectivity. Later, Lai et al. [17] accelerated the algorithm and remove foldings by applying the weighted Laplace–Beltrami eigen-projection. Several flow-based methods are proposed. Jin et al. [14] used Ricci flow to conformally deforms a genus-0 surface to a sphere, but Ricci flow is not strictly convex, which merely settles at a local minimum. Crane et al. [6] proposed Willmore flow for triangulated surfaces and applied it to spherical surface fairing. Recent years have seen the emergence of deep learning approaches for spherical surface data. Spherical CNNs [5,7] used rotation-equivariant convolutions to analyze spherical signals (e.g., climate models, molecular data), while Spherical U-Net [32,33] adapts U-Net for tasks like cortical surface parcellation in neuroimaging, employing spherical operations like surface convolution. These methods often treat surfaces as unstructured point sets, neglecting manifold geometry and topological properties, which cannot guarantee bijectivity. For instance, Zhao et al. [32] attempted bijectivity by learning the spherical diffeomorphic deformation field, but discretization errors can result in nonpositive Jacobian determinants, undermining strict bijectivity. Additionally, these approaches are typically task-specific and data-driven, and struggle with large-scale distortions or multiobjective optimization (e.g., balancing conformality and area preservation).

On the other hand, there are also works optimizing spherical self-mappings on the parametrization domain like [4, 13, 15, 23, 26, 27]. Isenburg et al. [13] and Kharevych et al. [15] cut meshes into two sections and obtained spherical results using stereographic mapping from plane to sphere. Choi et al. [4] based on quasiconformal theory, proposed a north pole–south pole iterative scheme to efficiently compute bijective landmark-aligned spherical harmonic parameterizations for genus-0 closed brain surfaces. Lyu et al. [27] applied similar ideas to computing spherical density equalizing parameterization for genus-0 surfaces. In the context of deep learning, Guo et al. [11] combined quasi-conformal geometry with CNNs to map triangular meshes with disk topology. They mapped two hemispheres to two new hemispheres and glued them seamlessly. However, these methods often impose fixed boundary constraints, such as prescribing boundaries in outer regions [4, 27] or requiring unchanged target domain geometry [11]. These constraints limit flexibility when adapting to complex surface features or tasks that require significant stretching.

In summary, existing methods face limitations in flexibility, theoretical rigor, or generality.

Numerical approaches lack adaptability due to fixed boundaries, whereas deep learning methods often ignore manifold structure and lack diffeomorphism guarantees. Our work builds on these insights, particularly improving mesh-based neural approaches to address these gaps effectively.

3. Contributions. Our work has several key contributions and novel aspects to the field of spherical parameterization, addressing the limitations of existing methods with a principled, free-boundary approach. Specifically, our contributions are as follows:

1. **BOOST: Beltrami Optimization On Spherical Topology for the large-deformation spherical mapping.** We introduce BOOST, a neural optimization framework for spherical/genus-0 surface mapping that splits the sphere into two hemispherical charts, optimizes the associated Beltrami fields in a free-boundary setting using a differentiable quasiconformal solver surrogate, and enforces global consistency via explicit boundary-matching, folding-avoidance, and seam-smoothing objectives. This divide-and-conquer strategy enables robust large deformations without imposing artificial fixed boundary constraints.
2. **Two-chart spherical Beltrami representation (spherical Beltrami differential) to formalize global consistency.** We define the spherical Beltrami differential as a pair of Beltrami fields on two stereographic charts together with the appropriate compatibility across charts, providing a concise representation of spherical self-quasiconformal maps (modulo conformal automorphisms) and a principled lens for controlling local distortion on the sphere.
3. **Beltrami-space optimization viewpoint for spherical diffeomorphic mapping problems.** We formulate spherical mapping tasks as direct optimization over Beltrami fields (rather than vertex coordinates), where the optimized variables encode intrinsic distortion. This leads to a flexible objective design that naturally supports diverse task terms (e.g., landmark alignment, feature-based matching) while maintaining distortion control.

As detailed in Sec.8, this framework successfully handles diverse applications including landmark matching and hybrid registration tasks, demonstrating its use in optimizing spherical self-mappings with bounded distortion and its robustness across challenging spherical mapping scenarios.

4. Mathematical Background.

4.1. Quasiconformal Mappings. Quasiconformal mappings generalize conformal mappings by extending orientation-preserving homeomorphisms to those with bounded conformality distortions. Mathematically, suppose Ω is a domain in \mathbb{C} , a mapping $f: \Omega \rightarrow \mathbb{C}$ is a quasiconformal map if it satisfies the Beltrami equation

$$(4.1) \quad \frac{\partial f}{\partial \bar{z}} = \mu(z) \frac{\partial}{\partial z}$$

for some measurable complex-valued function μ with $\|\mu\|_\infty < 1$, where $\frac{\partial f}{\partial z} = \frac{1}{2}(f_x - if_y)$ and $\frac{\partial f}{\partial \bar{z}} = \frac{1}{2}(f_x + if_y)$. μ is called the complex dilation or Beltrami coefficient of f , which measures the local deviation from a conformal map. Infinitesimally, around a point p , $f(p + z)$ might be

expressed as an affine map with negligible error $o(|z|)$:

$$(4.2) \quad f(p+z) \approx f(p) + f_z(p)z + f_{\bar{z}}(p)\bar{z} = f(p) + f_z(p)(z + \mu(p)\bar{z})$$

for a conformal map, its Taylor expansion excludes \bar{z} -terms, implying $\mu = 0$, and thus μ is a measure of nonconformality. Locally, f can be viewed as a composition of a translation to $f(p)$, a stretch map $S(z) = z + \mu(p)\bar{z}$, and a multiplication of $f_z(p)$. The stretch map $S(z)$ distorts a circle to an ellipse, with $\mu(p)$ determining the angles of maximal magnification ($\arg \mu/2$ with factor $1 + |\mu|$) and maximal shrinkage ($(\arg \mu + \pi)/2$ with factor $1 - |\mu|$).

Let $f: (x, y) \rightarrow (u, v)$ and $\mu = \rho + i\tau$, and denote by $\mathbf{S}(2)$ the space of all 2×2 symmetric positive definite matrices whose determinant is 1, then

$$(4.3) \quad D_f(z)^T D_f(z) = |\det D_f(z)|Q(z)$$

where $Q = (Q_{ij}): \Omega \rightarrow \mathbf{S}(2)$. Right multiplying both sides by $D_f(z)^{-1}$, we obtain a linear system which is the alternative formulation of the Beltrami equation:

$$(4.4) \quad \begin{bmatrix} u_x & u_y \\ v_x & v_y \end{bmatrix}^T = \text{sgn}(J_f(x)) \cdot \begin{bmatrix} q_{11} & q_{12} \\ q_{12} & q_{22} \end{bmatrix} \begin{bmatrix} v_y & -u_y \\ -v_x & u_x \end{bmatrix},$$

and from this we have $\mu = \frac{q_{11} - q_{22} + 2iq_{12}}{q_{11} + q_{22} + 2\text{sgn}(\det D_f)}$. With the constraint that $Q(z) \in \mathbf{S}(2)$, we observe that $|\mu(z)| < 1$ if and only if $\det D_f(z) > 0$. By inverse function theorem, researchers would through restricting $\|\mu\|_\infty < 1$, achieve local bijectivity and prevent folding in the triangular mesh [4, 22].

Suppose $\mu(z)$ is a measurable complex-valued function defined in a domain $U \subseteq \mathbb{C}$ for which $\|\mu\|_\infty < 1$, we have the following existence theorem.

Theorem 4.1. (Measurable Riemann Mapping Theorem) *For any function $\mu: U \rightarrow \mathbb{C}$ on with bounded essential supremum norm $\|\mu\|_\infty < 1$, there is a quasiconformal map ϕ on \overline{U} satisfying the Beltrami equation $\phi_{\bar{z}} = \mu\phi_z$ for almost all $z \in U$. Moreover, ϕ is unique up to post-composition with conformal isomorphisms and ϕ depends holomorphically on μ .*

For general Riemann surfaces, we have a similar concept, Beltrami differential.

Definition 4.2. *A Beltrami differential $\mu(z)\frac{dz}{dz}$ on a Riemann surface \mathcal{R} is an assignment to each chart z_α on U_α an \mathcal{L}_∞ complex-valued function μ_α defined on $z_\alpha(U_\alpha)$ such that*

$$\mu_\alpha(z_\alpha) = \mu_\beta(z_\beta) \frac{\overline{\left(\frac{dz_\beta}{dz_\alpha}\right)}}{\frac{dz_\beta}{dz_\alpha}}$$

and $\|\mu\|_\infty = \sup_\alpha \|\mu_\alpha\|_\infty$

The space of essentially bounded, complex-valued measurable Beltrami differentials on \mathcal{R} is a Banach space, denoted by $L_\infty(\mathcal{R})$. The open unit ball of $L_\infty(\mathcal{R})$ is denoted by $M(\mathcal{R})$. Elements $\mu = (\mu_\alpha)_\alpha$ in $M(\mathcal{R})$ are also called Beltrami coefficients.

4.2. Least Squares Quasi-conformal Energy. Apart from Eq.4.4, the Beltrami equation can be rewritten as

$$(4.5) \quad \begin{bmatrix} v_y \\ -v_x \end{bmatrix} = \frac{1}{1 - |\mu|^2} \begin{bmatrix} (\rho - 1)^2 + \tau^2 & -2\tau \\ -2\tau & (1 + \rho)^2 + \tau^2 \end{bmatrix} \begin{bmatrix} u_x \\ u_y \end{bmatrix}.$$

Here we assume $|\mu| < 1$ and for convenience, we denote the square matrix on the right-hand side by \mathbf{A} . Inspired by the least square conformal energy [20], Qiu [29] proposed the concept least square quasi-conformal (LSQC) energy of a map.

Definition 4.3. Let $\mu = \rho + ir$ be a complex-valued function defined on the domain Ω . The least squares quasi-conformal energy of the map $z = (x, y) \mapsto (u, v)$ against the Beltrami coefficient μ is defined to be

$$(4.6) \quad E_{LSQC}(u, v, \mu) = \frac{1}{2} \int_{\Omega} \|P \nabla u + J P \nabla v\|^2 dx dy,$$

where

$$P = \frac{1}{\sqrt{1 - |\mu|^2}} \begin{bmatrix} 1 - \rho & -r \\ -r & 1 + \rho \end{bmatrix}, J = \begin{bmatrix} 0 & -1 \\ 1 & 0 \end{bmatrix},$$

so that $P^T P = \mathbf{A}$ as in Eq.4.5 and $P^T J P = J$.

The LSQC energy admits the decomposition

$$(4.7) \quad E_{LSQC}(u, v, \mu) = E_{\mathbf{A}}(u; \Omega) + E_{\mathbf{A}}(u; \Omega) - \mathcal{A}(u, v)$$

where

$$E_{\mathbf{A}}(u; \Omega) = \frac{1}{2} \int_{\Omega} \nabla u^T \mathbf{A} \nabla u dx dy = \frac{1}{2} \int_{\Omega} \|P \nabla u\|^2 dx dy$$

is the Dirichlet-type energies of second-order equation $\nabla \cdot (\mathbf{A} \nabla u(z)) = 0$ derived by the decoupling method [22] and

$$(4.8) \quad \mathcal{A}(u, v) = \int_{\Omega} (u_y v_x - u_x v_y) dx dy.$$

is the area of the image.

Given a piecewise linear map $f(x, y) = u + \sqrt{-1}v$ and consider a triangle $T = (x_j, y_j)_{j=1,2,3}$ of \mathbb{R}^2 , we have

$$\begin{pmatrix} \partial u / \partial x \\ \partial u / \partial y \end{pmatrix} = \frac{1}{d_T} \begin{pmatrix} y_2 - y_3 & y_3 - y_1 & y_1 - y_2 \\ x_3 - x_2 & x_3 - x_1 & x_1 - x_2 \end{pmatrix} \begin{pmatrix} u_1 \\ u_2 \\ u_3 \end{pmatrix}$$

where $d_T = (x_1 y_2 - y_1 x_2) + (x_2 y_3 - y_2 x_3) + (x_3 y_1 - y_3 x_1)$ is twice the area of the triangle. The Beltrami equation (Eq.4.1) can be rewritten as $(1 - \mu)f_x + i(1 + \mu)f_y = 0$ and collected as a complex-valued linear system.

$$0 = \frac{i}{d_T} (W_1 \quad W_2 \quad W_3) (U_1 \quad U_2 \quad U_3)^{\top}$$

where $U_j = u_j + \sqrt{-1}v_j$ and

$$\begin{aligned} W_1 &= (1 + \mu)(x_3 - x_2) + \sqrt{-1}(1 - \mu)(y_3 - y_2) \\ W_2 &= (1 + \mu)(x_1 - x_3) + \sqrt{-1}(1 - \mu)(y_1 - y_3) \\ W_3 &= (1 + \mu)(x_2 - x_1) + \sqrt{-1}(1 - \mu)(y_2 - y_1). \end{aligned}$$

As a result,

$$\begin{aligned} E_{LSQC}(\mathbf{U} = (U_1, \dots, U_{|\mathcal{V}|})) &= \sum_{T \in \mathcal{T}} d_T \left| ((1 - \mu)f_x + i(1 + \mu)f_y) \right|_T^2 \\ &= \sum_{T \in \mathcal{T}} \frac{1}{d_T} \left| (W_{1,T} \quad W_{2,T} \quad W_{3,T})(U_{1,T} \quad U_{2,T} \quad U_{3,T})^\top \right|^2 \end{aligned}$$

and we may write as $E_{LSQC}(\mathbf{U}) = \|\mathcal{M}\mathbf{U}\|^2$ with $\mathcal{M} = (m_{ij}) \in \mathbb{C}^{|\mathcal{F}| \times |\mathcal{V}|}$ defined as

$$\mathcal{M}_{ij} = \begin{cases} w_{ij} = W_{j,T_i} & \text{if } j \text{ is a vertex of the face } T_i, \\ 0 & \text{otherwise.} \end{cases}.$$

To obtain a nontrivial solution, some of the U_i 's have to be pinned.

We decomposed $\mathbf{U} = (\mathbf{U}_f^\top, \mathbf{U}_p^\top)^\top$, where \mathbf{U}_f are free points, i.e. variables of the optimization problem, and \mathbf{U}_p are the points pinned. Similarly, we can decompose \mathcal{M} in blocked matrices as

$$\mathcal{M} = (\mathcal{M}_f, \mathcal{M}_p)$$

with $\mathcal{M}_f \in \mathbb{C}^{|\mathcal{F}| \times (|\mathcal{V}| - p)}$ and $\mathcal{M}_p \in \mathbb{C}^{|\mathcal{F}| \times p}$. Let 1 and 2 be real and imaginary parts of a complex number, and rewrite the $|\mathcal{F}|$ complex linear equations to $2|\mathcal{F}|$ real equations, we have

$$E_{LSQC}(\mathbf{U}) = \|\mathcal{A}\mathbf{u} - \mathbf{b}\|^2$$

where $\mathbf{u} = ((\mathbf{U}_f^1)^\top, (\mathbf{U}_f^2)^\top)^\top$ and

$$\mathcal{A} = \begin{pmatrix} \mathcal{M}_f^1 & -\mathcal{M}_f^2 \\ \mathcal{M}_f^2 & \mathcal{M}_f^1 \end{pmatrix}, \mathbf{b} = - \begin{pmatrix} \mathcal{M}_p^1 & -\mathcal{M}_p^2 \\ \mathcal{M}_p^2 & \mathcal{M}_p^1 \end{pmatrix} \begin{pmatrix} \mathbf{U}_p^1 \\ \mathbf{U}_p^2 \end{pmatrix}.$$

Finally, the nontrivial solution is $\mathbf{U} = \begin{pmatrix} (\mathcal{A}^\top \mathcal{A})^{-1} \mathcal{A}^\top \mathbf{b} \\ \mathbf{U}_p \end{pmatrix}$.

In the previous work [31], we prove multiple key properties of LSQC, listed as follows:

Proposition 4.4. (Nontriviality) Suppose $|\mu|$ is uniformly bounded away from 1, and the triangulation mesh is connected without dangling triangles. As long as $p \geq 2$, then \mathcal{A} has full rank.

Proposition 4.5. (Exact solution to Beltrami Equation) Suppose $|\mu|$ is uniformly bounded away from 1, and \mathbf{U} is the solution. If $|\mathcal{F}| = |\mathcal{V}| - 2$, then $\frac{\partial \mathbf{U}}{\partial \bar{z}} = \mu \frac{\partial \mathbf{U}}{\partial z}$.

Proposition 4.6. (Invariance by similarity transformation) *Given μ and pinned points \mathbf{U}_p and denote the corresponding free-point solution by \mathbf{U}_f , if the pinned points are transformed to $z\mathbf{U}_p + \mathbf{T}$ where $z \in \mathbb{C}$, $\mathbf{T} = (z', \dots, z')^\top \in \mathbb{C}^{|\mathcal{V}|}$, then the corresponding free-point solution is $z\mathbf{U}_f + \mathbf{T}$.*

Proposition 4.7. (Resolution independence) *Suppose we have a triangulation $\mathcal{T} = (\mathcal{V}, \mathcal{F})$ with piecewise constant $\mu = \{\mu_T : T \in \mathcal{F}\}$, and pinned points \mathbf{U}_p , and denote the corresponding solution by $\mathbf{U} = (\mathbf{U}_f, \mathbf{U}_p)$. Let $T = (\mathbf{v}_1, \mathbf{v}_2, \mathbf{v}_3)$ be a face in T and we split T into three triangles with $\mathbf{v} = \sum_{i=1}^3 \alpha_i \mathbf{v}_i$ ($\alpha_j > 0$) being the introduced vertex and T_i being the new triangles not containing \mathbf{v}_i as vertex. If $\mu_{T_i} = \mu_T$ ($i = 1, 2, 3$) and BCs on other faces remain, then the minimizer of this new minimization problem is $\mathbf{U}^+ = (\mathbf{U}^\top, \mathbf{U}_v)^\top$ where $\mathbf{U}_v = \sum_{i=1}^3 \alpha_i \mathbf{U}_i$.*

For detailed proofs, see [31].

5. Spherical Beltrami Differential and Spectral Beltrami Network. In this section, we present our theoretical contributions that form the mathematical foundation for neural-based spherical mapping optimization. We first establish fundamental correspondence results that extend the classical Beltrami theory to the spherical setting and then propose a Beltrami differential optimization framework for the problem, followed by introducing the Spectral Beltrami Network.

5.1. Spherical Beltrami Differential. Before stating a similar theorem on the relation between $M(\mathcal{R})$ and the space of quasiconformal maps between two Riemann surfaces, we give two lemmas.

Lemma 5.1. *Let f be a quasiconformal map from $\mathcal{R} = (U_\alpha, z_\alpha)_\alpha$ to $\mathcal{R}' = (V_\beta, w_\beta)_\beta$, then the Beltrami coefficients μ_α of $w_\beta \circ f \circ (z_\alpha)^{-1}$ determine an element μ in $M(\mathcal{R})$.*

Proof. Denote $w_\beta \circ f \circ (z_\alpha)^{-1}$ by $f_{\alpha\beta}$. We first need to prove that the Beltrami coefficients $\mu_{\alpha,\beta}$ of $f_{\alpha\beta}$ are independent of the choice of parameterizations w_β , thus can be denoted as μ_α .

Suppose β_1, β_2 are two charts such that $f(U_\alpha) \cap V_{\beta_1} \cap V_{\beta_2} \neq \emptyset$ and denote the intersection by $V_{\alpha,1,2}$. Then for $z \in z_\alpha^{-1} \circ f^{-1}(V_{\alpha,1,2})$, $\mu_{\alpha,\beta_1}(z) = (f_{\alpha,\beta_1})_{\bar{z}} / (f_{\alpha,\beta_1})_z$ and $\mu_{\alpha,\beta_2}(z) = (f_{\alpha,\beta_2})_{\bar{z}} / (f_{\alpha,\beta_2})_z$. If we denote the conformal transition $w_{\beta_2} \circ w_{\beta_1}^{-1}$ by w_{β_1,β_2} , then $f_{\alpha,\beta_2} = w_{\beta_1,\beta_2} \circ f_{\alpha,\beta_1}$ and by chain rule and $(w_{\beta_1,\beta_2})_{\bar{z}} = 0$, we have

$$\begin{aligned} \mu_{\alpha,\beta_2}(z) &= \frac{(w_{\beta_1,\beta_2})_z \cdot (f_{\alpha,\beta_1})_{\bar{z}} + (w_{\beta_1,\beta_2})_{\bar{z}} \cdot (\overline{f_{\alpha,\beta_1}})_{\bar{z}}}{(w_{\beta_1,\beta_2})_z \cdot (f_{\alpha,\beta_1})_z + (w_{\beta_1,\beta_2})_{\bar{z}} \cdot (\overline{f_{\alpha,\beta_1}})_z} \\ &= \frac{(w_{\beta_1,\beta_2})_z \cdot (f_{\alpha,\beta_1})_{\bar{z}}}{(w_{\beta_1,\beta_2})_z \cdot (f_{\alpha,\beta_1})_z} = \mu_{\alpha,\beta_1}(z) \end{aligned}$$

Next, show that the family of Beltrami coefficients induced by f satisfies the consistency requirement of Beltrami differential. Denote the conformal transition $z_{\alpha_2} \circ z_{\alpha_1}^{-1}$ by z_{α_1,α_2} , then

$f_{\alpha_1, \beta} = f_{\alpha_2, \beta} \circ z_{\alpha_1, \alpha_2}$ and we have

$$\begin{aligned}
 \mu_{\alpha_1}(z) &= \frac{(f_{\alpha_2, \beta} \circ z_{\alpha_1, \alpha_2})\bar{z}}{(f_{\alpha_2, \beta} \circ z_{\alpha_1, \alpha_2})z} = \frac{(f_{\alpha_2, \beta})_z \cdot (z_{\alpha_1, \alpha_2})\bar{z} + (f_{\alpha_2, \beta})\bar{z} \cdot (\overline{z_{\alpha_1, \alpha_2}})\bar{z}}{(f_{\alpha_2, \beta})_z \cdot (z_{\alpha_1, \alpha_2})z + (f_{\alpha_2, \beta})\bar{z} \cdot (\overline{z_{\alpha_1, \alpha_2}})z} \\
 &= \frac{(f_{\alpha_2, \beta})\bar{z} \cdot (\overline{z_{\alpha_1, \alpha_2}})\bar{z}}{(f_{\alpha_2, \beta})_z \cdot (z_{\alpha_1, \alpha_2})z + (f_{\alpha_2, \beta})\bar{z} \cdot (\overline{z_{\alpha_1, \alpha_2}})z} \\
 (5.1) \quad &= \frac{(f_{\alpha_2, \beta})\bar{z} \cdot \overline{(z_{\alpha_1, \alpha_2})z}}{(f_{\alpha_2, \beta})_z \cdot (z_{\alpha_1, \alpha_2})z + (f_{\alpha_2, \beta})\bar{z} \cdot (\overline{z_{\alpha_1, \alpha_2}})\bar{z}} \\
 &= \mu_{\alpha_2}(z) \frac{\overline{\left(\frac{dz_{\alpha_2}}{dz_{\alpha_1}}\right)}}{\frac{dz_{\alpha_2}}{dz_{\alpha_1}}}
 \end{aligned}$$

■

Therefore, a quasiconformal map would naturally determine a Beltrami differential on the domain surface, which is invariant under the parameterization of image.

Lemma 5.2. *Let $\mathcal{R} = (U_\alpha, z_\alpha)_\alpha$ be a Riemann surface and $\mu \in M(\mathcal{R})$, there exists a new atlas of charts $(U_\alpha, w_\alpha)_\alpha$ of the topological space \mathcal{R} such that the identity map $id : \mathcal{R} = (U_\alpha, z_\alpha)_\alpha \rightarrow \mathcal{R}^\mu = (U_\alpha, w_\alpha)_\alpha$ is quasiconformal with Beltrami coefficients μ .*

Proof. By Thm.4.1, there is a quasiconformal homeomorphism $f = f^\alpha$ defined on each $z_\alpha(U_\alpha)$ such that $f_{\bar{z}}(z) = \mu_\alpha(z)f_z(z)$. On each open set U_α of the given covering of \mathcal{R} , we introduce the new chart $w_\alpha = f^\alpha \circ z_\alpha$.

First, the transition maps for this new atlas satisfy

$$f_{\alpha\beta} = w_\alpha \circ (w_\beta)^{-1} = f^\alpha \circ (f^\beta \circ (z_\beta \circ z_\alpha^{-1}))^{-1}$$

by Eq.5.1, consider f^α and $f^\beta \circ (z_\beta \circ z_\alpha^{-1})$ on the overlapping regions in the $z_\alpha(U_\alpha)$, both are the solutions of the same Beltrami equations (with coefficients μ_α). By Thm.4.1, there exists a conformal map φ such that $f_\alpha = \varphi \circ (f^\beta \circ (z_\beta \circ z_\alpha^{-1}))$, and thus $f_{\alpha\beta} = \varphi$ is conformal.

Second, within this new system of charts, the identity map expressed in local coordinates is $w_\alpha \circ id \circ z_\alpha^{-1} = f^\alpha$ would satisfy the Beltrami equation with coefficients μ^α . ■

With these, we have the following existence theorem.

Theorem 5.3. *Let \mathcal{R} and \mathcal{R}' be two conformal structures of the unit sphere \mathbb{S}^2 , then for any $\mu \in M(\mathcal{R})$, there exists a quasiconformal mapping $f : \mathcal{R} \rightarrow \mathcal{R}'$ satisfying the Beltrami equation, which is unique up to the postcomposition of conformal mappings.*

Proof. Given $\mu \in M(\mathcal{R})$, by lemma 5.2, there exists a new chart \mathcal{R}^μ such that $id : \mathcal{R} \rightarrow \mathcal{R}^\mu$ is quasiconformal w.r.t μ . By uniformization theorem, there exists a conformal mapping $f : \mathcal{R}^\mu \rightarrow \mathcal{R}'$ and this conformal mapping is the desired quasiconformal mapping from \mathcal{R} to \mathcal{R}' . ■

By Uniformization Theorem, the result is still true in the more general case.

Corollary 5.4. *Let \mathcal{R} and \mathcal{R}' be two genus-0 closed surface, then for any $\mu \in M(\mathcal{R})$, there exists a quasiconformal mapping $f : \mathcal{R} \rightarrow \mathcal{R}'$ satisfying the Beltrami equation, which is unique up to the postcomposition of conformal mappings.*

Motivated by this, we define a simplified variant of Beltrami differential on the sphere.

Definition 5.5. A spherical Beltrami differential on \mathbb{S}^2 is a pair $\mu_{\mathbb{S}^2} = \{(\mu_N, U_N, P_N), (\mu_S, U_S, P_S)\}$ such that

- $U_N = \mathbb{S}^2 \setminus V_N$ where $V_N \subseteq \mathbb{S}^2$ is a neighborhood of the north pole. $P_N : U_N \rightarrow \mathbb{C}$ is the stereographic projection from the north pole.
- $U_S = \mathbb{S}^2 \setminus V_S$ where $V_S \subseteq \mathbb{S}^2$ is a neighborhood of the south pole. $P_S : U_S \rightarrow \mathbb{C}$ is the stereographic projection from the south pole.
- $U_N \cup U_S = \mathbb{S}^2$.
- μ_N is a Beltrami coefficient defined on $P_N(U_N) \subset \mathbb{C}$ and μ_S is a Beltrami coefficient defined on $P_S(U_S) \subset \mathbb{C}$ such that $\max\{\|\mu_N\|_\infty, \|\mu_S\|_\infty\} < 1$ and on the region $P_S(U_N \cap U_S)$, the coefficients satisfy:

$$\mu_S(z) = \mu_N(1/z) \cdot \left(\frac{\bar{z}}{z}\right)^{-2}$$

where $z \mapsto 1/z$ is the transition function $P_S \circ P_N^{-1}$.

By Thm.5.3, we establish a one-to-one correspondence between spherical self-quasiconformal maps and spherical Beltrami differentials, modulo the conformal automorphism group.

Corollary 5.6. Suppose $\mathcal{M} = \{(U_N, P_N), (U_S, P_S)\}$ is a conformal structure of spherical surface, then for any spherical Beltrami differential $\mu_{\mathbb{S}^2} = \{(\mu_N, U_N, P_N), (\mu_S, U_S, P_S)\}$, there exists a quasiconformal mapping $f : \mathcal{M} \rightarrow \mathbb{S}^2$ satisfying the Beltrami equation, which is unique up to the postcomposition of conformal mappings.

Our aim is to achieve spherical self-diffeomorphism optimization with explicit control in the local geometric distortion. Considering the correspondence between spherical Beltrami differentials and spherical self-quasiconformal maps, we may formulate the problem as optimization over these geometric quantities. Through stereographic projection, the diffeomorphic optimization problem for a spherical surface $\mathcal{M} = \{(U_N, P_N), (U_S, P_S)\}$ (Eq.1.1) can be reformulated as the optimization over spherical Beltrami differentials:

$$(5.2) \quad \begin{aligned} \min_{\mu=\mu_{\mathbb{S}^2}} \quad & E_1(f^\mu) + E_2(\mu) \\ \text{s.t.} \quad & f^\mu(\mathbb{S}^2) = P_N^{-1} \circ f^N \circ P_N(U_N) \cup P_S^{-1} \circ f^S \circ P_S(U_S) \\ & (f^N)_{\bar{z}} = \mu_N(f^N)_z, (f^S)_{\bar{z}} = \mu_S(f^S)_z \\ & \mu_S(z) = \mu_N(1/z) \cdot \left(\frac{\bar{z}}{z}\right)^{-2}, \quad z \in P_S(U_N \cap U_S) \end{aligned}$$

This new formulation includes two energy terms: E_1 drives task-specific objectives while E_2 regularizes BCs μ by constraining its magnitude (e.g., minimizing $|\mu|^2$) and smoothness (e.g., minimizing $|\nabla \mu|^2$). This dual-energy approach enables fine-tuned control over the quasiconformal mapping's geometric properties without compromising its task-oriented performance.

Due to Cor.5.6, above formulation is equivalent to

$$(5.3) \quad \begin{aligned} \min_{\mu=\mu_{\mathbb{S}^2}} \quad & E_1(f^\mu) + E_2(\mu) \\ \text{s.t.} \quad & f^\mu : \mathbb{S}^2 \rightarrow \mathbb{S}^2 \text{ is a homeomorphism} \\ & \mu_N = \mu(f^\mu|_{U_N}), \mu_S = \mu(f^\mu|_{U_S}) \end{aligned}$$

where $\mu(f|_U)$ is the Beltrami coefficient induced by the restriction of f on U . The Beltrami differential depends only on the domain surface's parameterization and for simplicity, in application we express the sphere self-mapping f in Eq.1.1 as $f: \mathbb{S}^2 = (P_S^{-1}(\bar{\mathbb{D}}), P_S) \cup (P_N^{-1}(\bar{\mathbb{D}}), P_N) \rightarrow \mathbb{S}^2 = (\Omega_1, P_N) \cup (\Omega_2, P_S)$, where P_S, P_N are south,north pole stereographic projections and Ω_j are simply connected domains in \mathbb{R}^2 . From this point of view, we can decompose f as the combination of its restriction on the upper and lower hemispheres, respectively. Equivalently, it can be viewed as the combination of two homeomorphisms on different hemispheres, and their images of the equator coincide. Therefore, the formulation is simplified to

$$(5.4) \quad \begin{aligned} \min_{\mu_S, \mu_N: \mathbb{D} \rightarrow \mathbb{C}} \quad & E_1(f^S, f^N) + E_2(\mu_S, \mu_N) \\ \text{s.t.} \quad & (f^N)_{\bar{z}} = \mu_N(f^N)_z, (f^S)_{\bar{z}} = \mu_S(f^S)_z, z \in \mathbb{D} \\ & P_S^{-1} \circ f^S(z) = P_N^{-1} \circ f^N\left(\frac{1}{z}\right), z \in \partial\mathbb{D} \end{aligned}$$

5.2. Spectral Beltrami Network. A key challenge is developing a differentiable tool to compute quasiconformal mappings from Beltrami differentials, enabling gradient-based optimization. Meanwhile, the mapping should be not subject to any Dirichlet type boundary constraints because the shape of the target domain $f^{\mu_\alpha} \circ z_\alpha(U_\alpha)$ is usually not prescribed. An important reason why LSQC is preferred in our work is that it implies that geometry of target domain is intrinsically determined by Beltrami coefficients and unlike decoupling methods [22] imposing a Dirichlet type boundary condition. This characteristic aligns seamlessly with the previously outlined Beltrami differential optimization formulation 5.4 and provides the flexibility to adjust boundary configurations dynamically through the optimization of the Beltrami differential.

Following the notation in [31], we can view the numerical LSQC algorithm as an operator \mathcal{F} . Let (V, F) be a triangulation of the unit disk, $\mu = \{\mu_T : T \in F\}$ be piecewise constant beltrami coefficients, $(p_i, q_i)_{i=1,2}$ be the two pairs of selected points in the mesh and their corresponding prescribed destinations in \mathbb{R}^2 , then the numerical solution $f = \mathcal{F}(\mu, p_1, p_2, q_1, q_2)$ such that $f(p_i) = q_i$ and $(\frac{\partial f}{\partial \bar{z}} / \frac{\partial f}{\partial z})|_T \approx \mu_T$. For the aim of applying LSQC to gradient-based optimization problems, Spectral Beltrami Network (SBN) is proposed in the previous paper. Given Beltrami coefficients $\{\mu_v : v \in V^1\}$ defined for vertices on a prescribed mesh of \mathbb{D} (or equivalently a directed graph) $\mathcal{G}^1 = (V^1, E^1, F^1)$ and coordinates of two pinned points (p_1, p_2) , SBN would predict the mapping $f(V^1)$ such that $f(V^1) \approx \mathcal{F}(\mu, p_1, p_2, p_1, p_2)$ where $\mu = \{\mu_T : \mu_T = \frac{1}{3} \sum_{v \in T} \mu_v, T \in F^1\}$. For capturing short-range and long-range information exchange between distinct vertices in the mesh, SBN couples mesh spectral layers with the multiscale message passing mechanism. The mesh spectral layer is to project the latent feature vectors into a span of low-frequency mesh Laplacian eigenvectors, do the multinode linear transformation in the frequency domain followed by an inverse projection back to the spatial domain, through which global shape context is injected to the latent space. In addition, the multiscale mesh hierarchy can widen the receptive field without exploding memory, improving the efficiency of information exchange through downsampling and upsampling. Fig.1 shows the architecture of SBN. For more details about the network, please refer to [31].

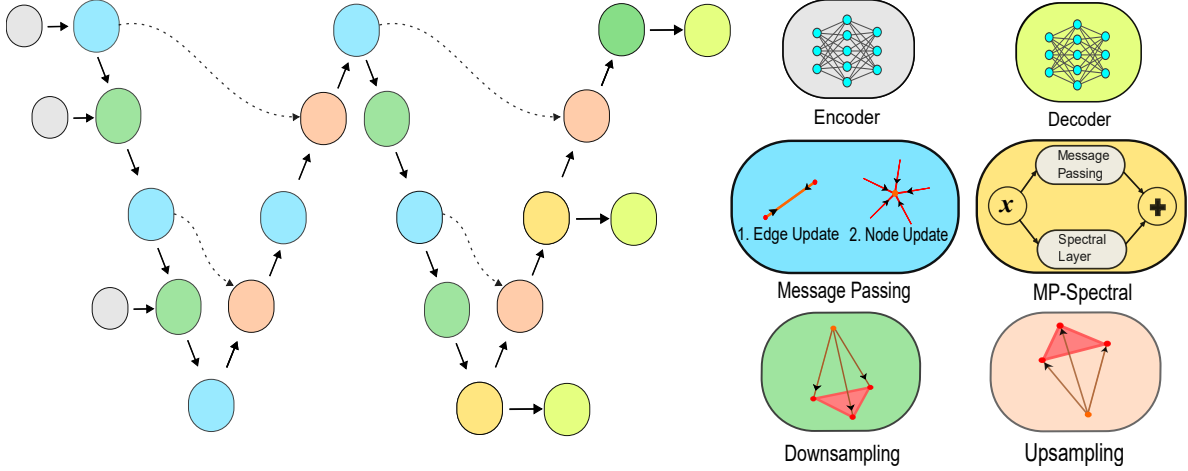


Figure 1: *Architecture of Spectral Beltrami Network*

6. Beltrami Optimization On Spherical Topology (BOOST). Since we have the Spectral Beltrami Network (SBN) which can predict free-boundary diffeomorphisms on the unit disk \mathbb{D} , in the following, we introduce the optimization framework BOOST for the general spherical parameterization problem, which incorporates SBN for freely deforming the 2D parameterization domain.

The SBN model serves as a tool for spherical surface parameterization, transforming a hemisphere into a submanifold of the unit sphere. By optimizing the Beltrami coefficients (BCs) and the coordinates of two fixed points—followed by post-composition with scaling, rotation, and translation—we derive optimal mappings tailored to specific tasks.

To ensure valid inputs, the input BCs and fixed points must have norms less than 1. Let $\tilde{\mu}_v$, T_{BC} , \tilde{p}_i and T_{pin} be the parameters to be optimized, then define an activation function \mathcal{T}

$$\mathcal{T}(x, T) = \left(\frac{e^{\frac{|x|}{T}} - e^{-\frac{|x|}{T}}}{e^{\frac{|x|}{T}} + e^{-\frac{|x|}{T}}} \right) e^{i \arg(x)}$$

and $\mu_v = \mathcal{T}(\tilde{\mu}_v, T_{BC})$ and $p_i = \mathcal{T}(\tilde{p}_i, T_{pin})$ are the input to the model.

Now, we propose an optimization framework for spherical mapping problems, which jointly optimizes the mappings of both hemispheres via SBN, **B**eltrami **O**ptimization **O**n **S**pherical **T**opology (abbreviated as **BOOST**).

Let $\mathcal{G} = (V^1, F^1)$ be the standard mesh where SBN \mathcal{F}_θ works, and $\mathcal{F}_\theta(\mu, p_1, p_2)$ be the structured output of SBN given $\mu = \{\mu_v : v \in V^1\}$ and two fixed points p_1, p_2 .

Given a spherical surface mesh S , we divide it into two hemispheres, upper S_{upp} and lower ones S_{low} based on the signs of z -coordinates. Apply south (P_S) and north (P_N) pole stereographic projection to the S_{upp} and S_{low} , respectively, we obtain 2D triangular mesh $D_{upp} \in \mathbb{R}^{|V_{upp}| \times 2}$ and $D_{low} \in \mathbb{R}^{|V_{low}| \times 2}$ within the unit disk \mathbb{D} . SBN, operating on a standard mesh $\mathcal{G} = (V^1, F^1)$, predicts mapping $f^S = \mathcal{F}_\theta(\mu_S, p_{S,1}, p_{S,2})$ and $f^N = \mathcal{F}_\theta(\mu_N, p_{N,1}, p_{N,2})$. With barycentric interpolation, we can obtain deformation of D_{upp} and D_{low} , and finally use

inverse projection P_S^{-1}, P_N^{-1} to reconstruct the hemispheres. Sometimes, for simplicity, we may use spherical barycentric interpolation as an alternative. Essentially, the key point is to find a smooth and bijective sphere self-mapping that works on the standard spherical mesh $P_S^{-1}(V^1) \cup P_N^{-1}(V^1 \setminus \partial V^1)$ such that the interpolated result minimizes the loss objective.

The optimization needs to ensure: (1) no overlaps when gluing the hemispheres, and (2) minimal boundary mismatch. Specifically, there must be no overlaps around the boundaries of two transformed hemispheres when gluing back, meanwhile the distance between $P_S^{-1}(f^S(v))$ and $P_N^{-1}(f^N(v))$ for each $v \in \partial V^1$ should be small enough. For the second goal, we propose a boundary matching loss

$$\mathcal{L}_{\text{bm}}(f^S, f^N) = \frac{1}{|\partial V^1|} \sum_{v \in V^1} \|P_S^{-1}(f^S(v)) - P_N^{-1}(f^N(v))\|_2^2$$

For the first aim, our idea is that if there are overlaps when gluing back, replacing $P_N^{-1}(f^N(\partial V^1))$ in $P_N^{-1}(f^N(V^1))$ by $P_S^{-1}(f^S(\partial V^1))$, and denoting this new image by $\tilde{\mathcal{M}}$, folding would occur in $P_N(\tilde{\mathcal{M}})$, which results that let f be the facewise linear mapping from V^1 to $\tilde{\mathcal{M}}$, Jacobian determinants of some triangular faces would be negative. Folding in $\tilde{\mathcal{M}}$ is penalized by

$$\mathcal{L}_{\text{folding}}(\tilde{\mathcal{M}}) = \int_{\Omega^-} \det(J_f) dx dy \approx \frac{1}{|F^1|} \sum_{T \in F^1} \phi(-\det(J_f(T)))$$

where ϕ is the ReLU function, Ω^- is the set of points whose Jacobian determinant is negative and J_f is the Jacobian determinant of the mapping $f: V^1 \rightarrow \tilde{\mathcal{M}}$.

The last thing is to ensure the smoothness of the boundary of the structured mesh $\tilde{\mathcal{M}}$, because its boundary points and inner points are from distinct outputs. Let L_1 be the circle of points inside $f^S(V^1)$ which is adjacent to the boundary points $f^S(\partial V^1)$ and L_2 be the circle of points inside $f^N(V^1)$ which is adjacent to the boundary points $f^N(\partial V^1)$, we define a new mesh \mathcal{N} by combining $P_N(\tilde{\mathcal{M}})$ with $P_N \circ P_S^{-1}(L_1)$. By the construction of \mathcal{N} , we know $P_N \circ P_S^{-1}(f^S(\partial V^1))$ and $P_N \circ P_S^{-1}(L_1)$ are results from the upper hemisphere, L_2 are results from the lower hemisphere, so for the ring of a point $v \in P_N \circ P_S^{-1}(f^S(\partial V^1))$, its adjacent faces are not output from one hemisphere, so there might be inconsistency in this ring. In our mesh, each point $v \in P_N \circ P_S^{-1}(\partial V^1)$ has a one-ring neighborhood consisting of six triangular faces that share this point as a vertex. These six triangles are split evenly: three belong to the upper hemisphere and three belong to the lower hemisphere. Since we deform each hemisphere independently, the mapped positions of these six triangles in the parameter space may not align consistently. Hence we impose a boundary smoothness loss on the Laplacian and double Laplacian of the boundary points.

$$\mathcal{L}_{\text{bs}} = \sum_{v \in P_N \circ P_S^{-1}(f^S(\partial V^1))} \|\Delta^2 v\|_2^2 + 0.1 \cdot \|\Delta v\|_2^2$$

where $\Delta v_i = \sum_{[i,j]} \omega_{ij} (v_j - v_i)$ and $\omega_{ij} = \frac{1}{2}(\cot \alpha_{ij} + \cot \beta_{ij})$, α_{ij} and β_{ij} are the angles opposite to the edge $[i, j]$, and Δ^2 is the standard scalar Laplacian applied twice. The double Laplacian term distributes the derivative change smoothly into the interior, preventing tension discontinuities. An illustration of \mathcal{L}_{bm} , $\mathcal{L}_{\text{folding}}$ and \mathcal{L}_{bs} is given in Fig.2

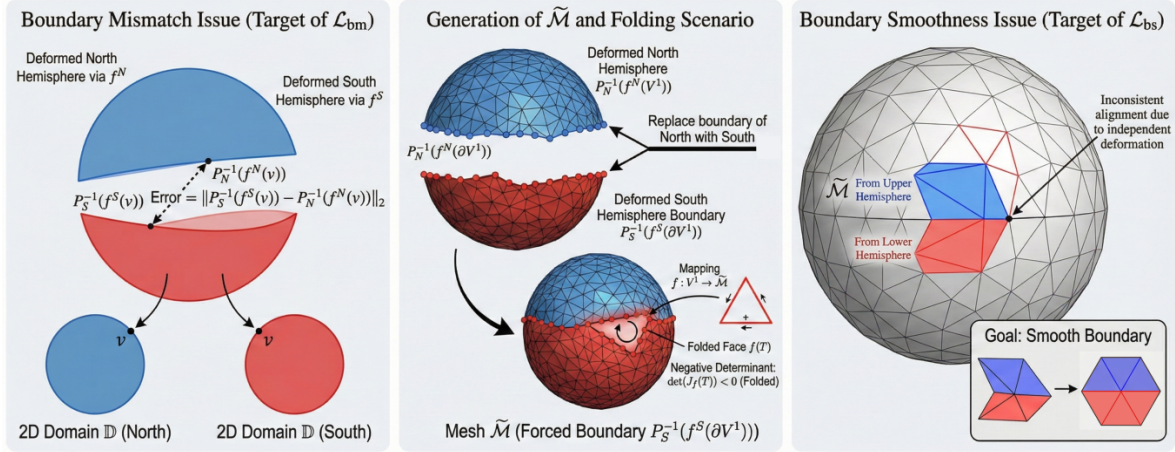


Figure 2: Illustration of three issues addressed by the loss functions \mathcal{L}_{bm} , $\mathcal{L}_{\text{folding}}$ and \mathcal{L}_{bs}

In all, let us denote the post-composition of similarity transformation by $g(x, \phi, \varphi, r) = \varphi e^{i\phi} x + r$ and after training of SBN is done, we freeze its parameter and obtain \mathcal{F}_{θ^*} , whose output $\mathcal{F}_{\theta^*}(\{\mu_v\}, p_1, p_2) \approx \mathcal{F}(\{\mu_F\}, p_1, p_2, p_1, p_2)$. And we can reformulate the framework 5.4 and obtain BOOST as follows

$$(6.1) \quad \begin{aligned} \min_{(T_{\text{BC}}, T_{\text{pin}}, \theta_N, \theta_S)} & \lambda_{\text{task}} \mathcal{L}_{\text{task}}(f^S, f^N) + \lambda_{\text{reg}} \mathcal{L}_{\text{reg}}(\theta_S, \theta_N) \\ & + (\lambda_{\text{bm}} \mathcal{L}_{\text{bm}} + \lambda_{\text{bs}} \mathcal{L}_{\text{bs}} + \lambda_{\text{folding}} \mathcal{L}_{\text{folding}})(f^S, f^N) \end{aligned}$$

where $\theta_N = \{\tilde{\mu}_N, \tilde{p}_{N,1}, \tilde{p}_{N,2}, \phi_N, s_N, r_N\}$ and $\theta_S = \{\tilde{\mu}_S, \tilde{p}_{S,1}, \tilde{p}_{S,2}, \phi_S, \varphi_S, r_S\}$ are the parameter sets and

$$\begin{aligned} f^S &= g(\mathcal{F}_{\theta^*}(\mu_S, p_{S,1}, p_{S,2}), \phi_S, \varphi_S, r_S), \\ f^N &= g(\mathcal{F}_{\theta^*}(\mu_N, p_{N,1}, p_{N,2}), \phi_N, \varphi_N, r_N). \end{aligned}$$

Last, the regularization term \mathcal{L}_{reg} is designed to discourage local geometric distortion and enhance the smoothness of the mapping. Therefore, two regularization terms are always used in \mathcal{L}_{reg} , defined as

$$\begin{aligned} \mathcal{L}_{\text{BC}} &= \frac{1}{|V^1|} \sum_{v \in V^1} (|\mu_S(v)|^2 + |\mu_N(v)|^2) \\ \mathcal{L}_{\text{smooth}} &= \frac{1}{|F^1|} \sum_{T \in F^1} (|\nabla \mu_S(T)|^2 + |\nabla \mu_N(T)|^2) \end{aligned}$$

The details discussed are summarized in Alg.6.1.

7. Implementation. For the training detail of the SBN model, please refer to [31]. In downstream applications, besides manually designing the weight of each loss term, we may treat this multi-loss optimization as a multitask learning problem. To balance the optimization

Algorithm 6.1 Beltrami Optimization On Spherical Topology

Input: Data: A triangular mesh of unit sphere \mathbb{S}^2 .

1. optimization parameters $\eta: T_{\text{BC}}, T_{\text{pin}}, \theta_N = \{\tilde{\mu}_N, \tilde{p}_{N,1}, \tilde{p}_{N,2}, \phi_N, s_N, r_N\}$ and $\theta_S = \{\tilde{\mu}_S, \tilde{p}_{S,1}, \tilde{p}_{S,2}, \phi_S, \varphi_S, r_S\}$,
2. loss weights λ_j , loss functions \mathcal{L}_j , optimizer Ψ

Output: transformed spherical mesh \tilde{S}

- 1: Freeze the parameters of SBN \mathcal{F}_{θ^*} .
- 2: *continue* = *True*;
- 3: **while** *continue* **do**
- 4: Prepare input $\mu = \mathcal{T}(\tilde{\mu}, T_{\text{BC}}), p_i = \mathcal{T}(\tilde{p}_i, T_{\text{pin}})$ for the model \mathcal{F} .
- 5: Compute two mappings predicted by model, $f^S = g(\mathcal{F}_{\theta^*}(\mu_S, p_{S,1}, p_{S,2}), \phi_S, \varphi_S, r_S)$ and $f^N = g(\mathcal{F}_{\theta^*}(\mu_N, p_{N,1}, p_{N,2}), \phi_N, \varphi_N, r_N)$.
- 6: Obtain the deformed spherical surface mesh \tilde{S} via interpolation on f^S, f^N .
- 7: Compute the weighted sum $\mathcal{L}_{\text{total}}$ of losses $\mathcal{L}_{\text{task}}(\tilde{S}), \mathcal{L}_{\text{reg}}(\theta_S, \theta_N), \mathcal{L}_{\text{bm}}, \mathcal{L}_{\text{bs}}, \mathcal{L}_{\text{folding}}$ and $\mathcal{L}_{\text{smooth}}$ with weights λ_j .
- 8: **if** $\mathcal{L}_{\text{total}}$ and each individual loss meet stop criterion **then**
- 9: *continue* = *False*;
- 10: **else**
- 11: Compute $\frac{\partial \mathcal{L}_{\text{total}}}{\partial \eta}$ for all parameters η to be optimized and then update all η with the optimizer Ψ .
- 12: **end if**
- 13: **end while**

of multiple loss terms, we adapted the method from [21] with modifications. Specifically, we introduced learnable loss weights c_i to dynamically adjust the emphasis on each task. Loss terms below predefined thresholds were excluded from optimization to focus on more challenging tasks, preventing the model from overfitting to simpler objectives. This approach is detailed in Alg.7.1. All experiments were conducted on an NVIDIA A40 GPU with 44GB memory, ensuring efficient computation.

8. Experimental results. Numerical experiments were conducted to evaluate the efficacy of our framework BOOST, which composed of several applications in landmark, intensity, and hybrid registration problems, encompassing both realistic and synthetic scenarios.

8.1. Cortical Surface Registration. To further demonstrate the versatility and effectiveness of our framework, we conducted a series of experiments focusing on the spherical parameterization of cortical surfaces. We tested Alg.6.1 by performing a landmark alignment task on the spherical parameterization of right cortical surface data. We followed the experiment setup from FLASH [4]. On each cortical surface, there are six landmark curves, including Central Sulcus (CS), Inferior Frontal Sulcus (IFS), Superior Frontal Sulcus (SFS), Inferior Temporal Sulcus (ITS), Superior Temporal Sulcus (STS) and Postcentral Sulcus (PostCS). We first used FLASH [4] to obtain a spherical conformal parameterization of each cortical surface and aligned landmarks on the pair of spherical cortical surfaces. Mathematically, denote six landmark curves on the spherical parameterization of two cortical surfaces by

Algorithm 7.1 multi-task loss with threshold

Input: 1. Output f and input μ, p of the SBN and parameters (θ, σ, t) in post-composed mapping.
2. loss functions \mathcal{L}_i , corresponding thresholds \mathcal{N}_i and learnable loss weights $c_i, (i = 1, 2, \dots, n)$

Output: loss \mathcal{L}_{total}

```

1:  $\mathcal{L}_{total} = 0$ 
2: for  $i = 1$  to  $n$  do
3:   Compute  $\mathcal{L}_i = \mathcal{L}_i(f, \mu, p, \theta, \sigma, t)$ 
4:   if  $\mathcal{L}_i > \mathcal{N}_i$  then
5:      $\mathcal{L}_{total} = \mathcal{L}_{total} + c_i \mathcal{L}_i$ 
6:   end if
7: end for
```

$S_{1,i}, S_{2,i} (i = 1, \dots, 6)$ and similarity measure functions of landmark pairs to be matched by d_{sim} . Our goal is to find $f: \mathbb{S}^2 \rightarrow \mathbb{S}^2$ such that

1. minimizing $d_{sim}(S_{1,i}, S_{2,i})$ for all $i = 1, \dots, 6$;
2. f is diffeomorphic;
3. f is geometrically regularized.

The goal is formulated as finding an optimal mapping f minimizing an energy functional

$$\mathcal{L}_{lm}(f) = \mathcal{L}_{task}(f) + \mathcal{L}_{reg}(f),$$

where

$$\mathcal{L}_{task}(f) = \frac{1}{6} \sum_{i=1}^6 d_{sim}(f(S_{1,i}), S_{2,i}).$$

For the regularization terms involved in included but not limited to this experiment, we usually use a weighted sum of $\mathcal{L}_{bm}, \mathcal{L}_{folding}, \mathcal{L}_{bs}, \mathcal{L}_{\mu}$ and \mathcal{L}_{sm} .

In prior work [4], d_{sim} is nodewise L2 square distance and this is indispensable for them to linearize the optimization problem via the variational method. To satisfy this, Choi et.al [4] used resampling to ensure that the number of nodes in the corresponding curves is the same. We applied the same resampling operation, followed by a rotation to minimize the average landmark L2 distance. The registration was then performed using our SBN-based framework, and the results were compared with those of FLASH [4] in terms of both angle distortion and landmark matching error. Numerical results show that our method achieves competitive, or even superior, landmark matching accuracy meanwhile always yielding consistently lower angle distortions. Fig.3 and Fig.4 compare the performance of different methods in an example of registering brain 32 to brain 35, in terms of visual effect and statistics of induced Beltrami coefficients. See Tab.1 for a more comprehensive comparison.

Moreover, in both experimental and real-world brain landmark matching tasks, it is impractical to require that corresponding curves from different brains have the same number of points. Curves like the Central Sulcus of different brains may be represented by different numbers of sampled points due to variations in brain size, shape, or imaging resolution.

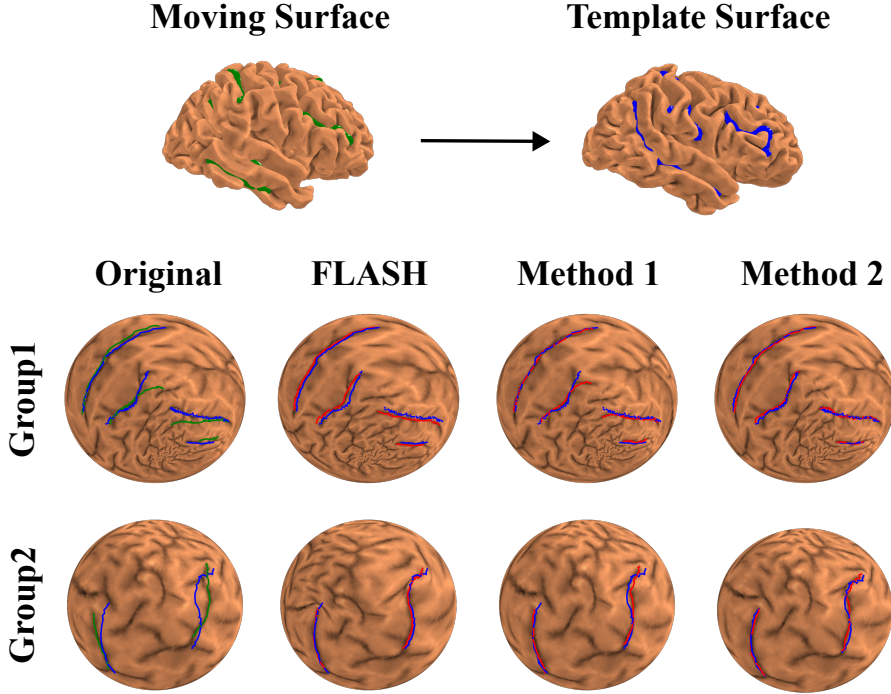


Figure 3: Registration results for brain 32 to brain 35 using six sulcal landmarks. Landmarks are grouped (Group 1: CS, ITS, STS, postCS; Group 2: IFS, SFS) for visual clarity. Columns, from left to right: source/target landmark pairs (green: moving surface, blue: template), followed by results from FLASH [4], our method with resampling, and our method with chamfer distance. Red shows deformed sulci, blue shows targets.

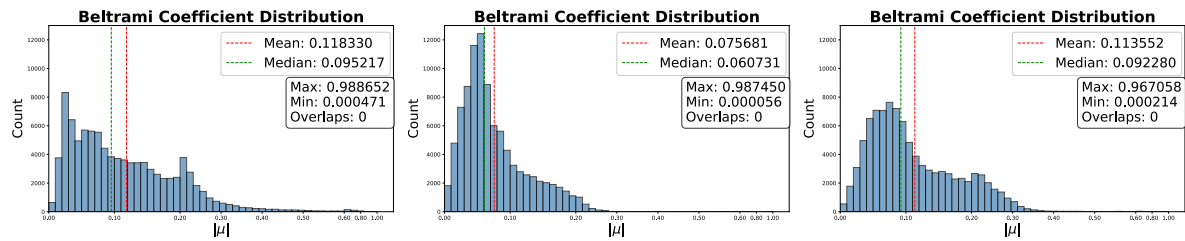


Figure 4: Comparison of induced angle distortion for three methods; FLASH [4] (Left), our method with landmark resampling (Middle), and our method using chamfer distance (Right), represented by distributions of Beltrami coefficients associated with deformation.

This discrepancy poses a significant challenge for traditional alignment methods that rely on point-to-point comparisons. Additionally, if the same curves in two subjects indeed have very different lengths, as the following large deformation case indicates, these resampling methods

surface	FLASH [4]				method 1				method 2			
	Number of overlaps	Mean $ \mu $	Mean Square distance	Mean chamfer distance	Number of overlaps	Mean $ \mu $	Mean Square distance	Mean chamfer distance	Number of overlaps	Mean $ \mu $	Mean Square distance	Mean chamfer distance
Brains 35 and 32	0	0.118	0.0017	0.0015	0	0.103	0.0009	0.0011	0	0.114	0.0031	0.0009
Brains 22 and 28	0	0.407	0.0038	0.0004	0	0.098	0.0030	0.0036	0	0.258	0.0021	0.0002
Brains 29 and 13	1	0.493	0.0031	0.0030	0	0.108	0.0037	0.0043	0	0.119	0.0054	0.0009
Brains 8 and 18	5	0.548	0.0047	0.0083	0	0.085	0.0042	0.0047	0	0.110	0.0079	0.0018
Brains 32 and 2	0	0.372	0.0037	0.0075	0	0.103	0.0030	0.0032	0	0.116	0.0028	0.0006

Table 1: Comparison of landmark matching performance and angle distortion among FLASH [4] and BOOST (with two variations: method 1—with landmark resampling; method 2—using chamfer distance as loss, without landmark resampling). For each pair of brains, the table provides the number of overlap failures, average $|\mu|$, mean squared distance, and mean chamfer distance. Lower values are better in all columns except number of overlaps.

may not accurately capture true anatomical correspondence, potentially introducing errors and artifacts, affecting the reliability of subsequent analyzes.

An advantage of our framework is its flexibility to incorporate with any differentiable loss functions. By treating each pair of curves to be matched as two point clouds, we can adopt the chamfer distance as the loss function. Let S_1 and S_2 be two point clouds, and their chamfer distance is defined by

$$d_{CD}(S_1, S_2) = \frac{1}{|S_1|} \sum_{y \in S_1} \min_{x \in S_2} \|x - y\|^2 + \frac{1}{|S_2|} \sum_{x \in S_2} \min_{y \in S_1} \|y - x\|^2.$$

For better performance, we also required that two endpoints of each curve on the moving surface can be matched with those of its target. Suppose $q_{1,i}, q_{2,i}$ are endpoints of i -th curves in S_1 and $t_{1,i}, t_{2,i}$ are their targets, then

$$\mathcal{L}_{task}(f) = \frac{1}{6} \sum_{i=1}^6 d_{CD}(f(S_{1,i}), S_{2,i}) + \frac{1}{12} \sum_{i=1}^6 \sum_{j=1}^2 |q_{j,i} - t_{j,i}|^2.$$

For clarity, we denote the former application of our framework by method 1, and this by method 2. A result is shown in the rightmost column of Fig.3. As Tab. 1 shown, Replacing the L2 nodewise distance by the sum of the chamfer distance and endpoint loss consistently achieves visually better landmark matching performance and smaller angle distortion than FLASH [4].

In addition, even when the initial landmark distortion is small, FLASH [4] may fail to achieve a diffeomorphic deformation when imposing too many landmark constraints, whereas our method remains robust. For example, when registering brain 8 (moving surface) to brain 18 (template surface), FLASH is able to handle registering ITS and STS, or CS, SFS, IFS, and postCS separately, but cannot provide a diffeomorphic registration when all six sulci are involved. In contrast, our method can simultaneously register all six landmark curves, and the registration accuracy for both ITS and STS, as well as CS, SFS, IFS, and postCS, exceeds that of FLASH even when FLASH handles these sulci in individual smaller groups. As shown in Fig.5, compared to FLASH, we can match the landmark curve well without inducing too

much distortion in other regions. For example, the ITS-STS registration result by FLASH is highly biologically implausible, whereas ours induces much less distortion in regions away from landmark curves, no matter whether using landmark resampling or not. Our another advantage

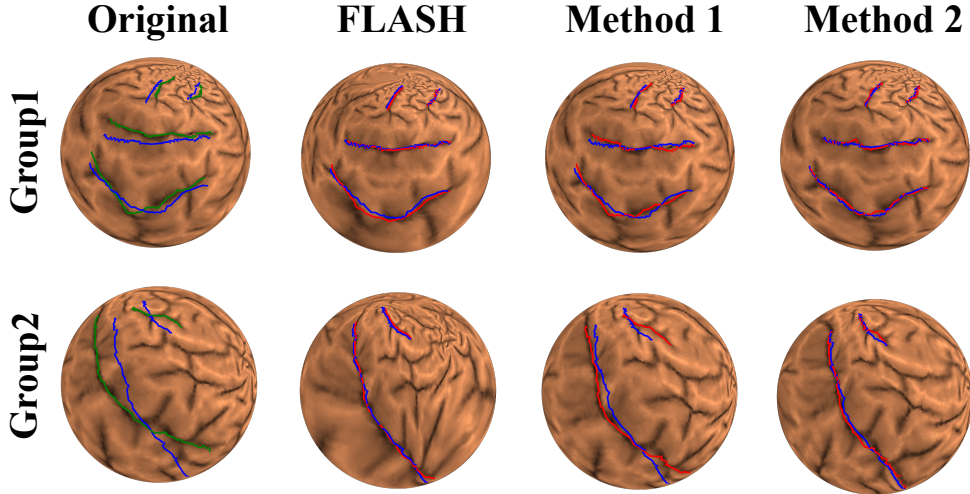


Figure 5: *Registration of brain 8 to brain 18 with 6 sulcal landmarks (for visualization and color conventions, see Fig. 3). Note that in this figure, first row is visualization of CS, IFS, SFS and postCS, while the second row is visualization of ITS and STS. The second column are two independent results done by FLASH [4], respectively.*

is that it remains robust in the large deformation case. See Fig.6 for an example registering CS, IFS and SFS of brain 39 to those of brain 35. As shown, there are big differences between lengths and positions between two curves in each landmark pair. FLASH [4] fails to give a non-overlap deformation while ours still provides a diffeomorphic registration result with little distortion.

Furthermore, our method is seamlessly compatible with geometric feature alignment in anatomical parcellation. For illustration, we registered 16 subjects' right-hemi cortical surface in the OASIS dataset [19] to population averages from FreeSurfer [8]. More detailedly, initial spherical representations for each subject's cortical surface were generated using FreeSurfer. We designated the fsaverage6 surface, a standard population-average spherical template distributed with FreeSurfer, as the common registration target space. For the parcellation registration, we used FreeSurfer to generate parcellation labels (i.e. 34 cortical areas) for each subject including the fsaverage6 surface. A preprocessing step involves mapping subject-specific geometric features (e.g., sulcal depth, curvature, or other relevant anatomical descriptors) from the individual's native spherical parameterization onto the fsaverage6 template. This is achieved by interpolating these feature values at the vertex locations defined by the fsaverage6 mesh. This procedure ensures that feature information from the moving subject is represented on the common template grid, establishing vertex-wise correspondence for comparative analysis and

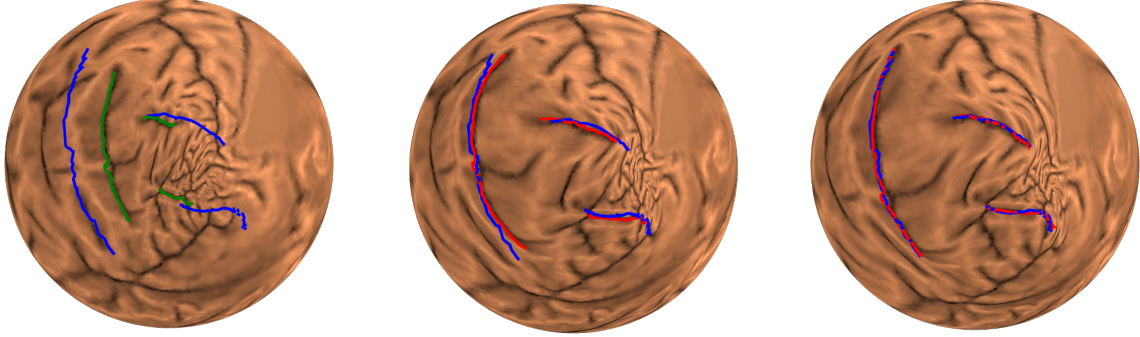


Figure 6: *Registration of brain 39 to brain 35 using CS, IFS, SFS as landmark curves (for color conventions, see Fig.3). The first column is visualization on the original moving face. The second and third ones are results using method 1 and 2, respectively.*

guiding the alignment.

Let Φ be the non-rigid deformation, and M, F be geometric features on the moving sphere and the fixed sphere, respectively. During optimization, the feature similarity between $M \circ \Phi$ and F is estimated using Pearson correlation coefficient(PCC),

$$d_{corr}(M \circ \Phi, F) = \frac{cov(M \circ \Phi, F)}{\sigma(M \circ \Phi)\sigma(F)}.$$

For the parcellation alignment, we leveraged the Dice score of anatomical parcellation between the moved and fixed spheres:

$$\text{Dice}(M^p \circ \Phi, F^p) = \frac{2 \cdot |M^p \circ \Phi \cap F^p|}{|M^p \circ \Phi| + |F^p|},$$

where M^p and F^p are the parcel p in the moving and fixed spheres. The parcellation loss is

$$d_{par}(M \circ \Phi, F) = \frac{1}{P} \sum_{i=1}^P (1 - \text{Dice}(M^p \circ \Phi, F^p)),$$

where P denotes the number of parcels, and the parcellation atlas used in registration are all generated by FreeSurfer.

Again, we applied BOOST with $\mathcal{L}_{task} = 4 \cdot d_{par} + d_{corr}$ for the experiment. The parcellation accuracy was quantified using the Dice score (higher values denote greater overlap). The alignment of geometric features was evaluated by comparing each subject's sulcal depth to the FreeSurfer fsaverage atlas. Similarity was measured via PCC, with higher PCC indicating better alignment. Our method achieves 0.8844 PCC for sulci depth on average and 0.9680 Dice score on average, and Fig.8a shows a more detailed result for 34 regions parceled by the atlas provided by FreeSurfer. Note that to the best of our knowledge, there have not been works conducting the same experiments on the OASIS3 dataset before, and the aim of this experiment is to demonstrate the flexibility and capacity of our method and its potential to be

widely applied in many tasks. So, it is not our intention to focus on comparing the performance with others. However, it is worth mentioning that in SUGAR [30], Ren et al. conduct the same experiment on the ADRC dataset, which also consists of brain data from Alzheimer Disease subjects, and their method achieved 0.839 Dice score and 0.904 PCC. This implies that our method is also competitive and potentially superior to other mainstream algorithms.

8.2. Extreme Distortion. We further challenge our method by conducting a synthetic and highly demanding landmark-matching experiment designed to create extreme distortions. Specifically, we randomly selected $2n$ ($n = 2, 3, 4$) groups of landmarks $(A_i, B_i, C_i, D_i)_{i=1,2,\dots,2n}$, distributed evenly on both hemispheres. Each group of landmarks is constrained that adjacent points are mapped to each other, thereby constructing $2n$ large-scale twists on the spherical surface. The first row of Fig.7 displays representative pairs of landmarks, while the task loss in this setup is defined as

$$\begin{aligned}\mathcal{L}_{task}(\mu, p) = & \frac{1}{8n} \sum_{i=1}^n (|\mathcal{F}(\mu, p)(A_i) - B_i|^2 + |\mathcal{F}(\mu, p)(B_i) - C_i|^2 \\ & + |\mathcal{F}(\mu, p)(C_i) - D_i|^2 + |\mathcal{F}(\mu, p)(D_i) - A_i|^2).\end{aligned}$$

Fig.7 is a result of $n = 4$ and the average L2 squared error of each pair is decreased to $7.96 \times e^{-4}$ after optimization. As demonstrated by the qualitative and quantitative results, SBN is highly adept at dealing with tasks requiring extremely large deformation mappings: bijectivity is rigorously preserved since all Beltrami coefficients retain a norm less than 1 throughout, while smoothness and conformality are maintained by constraining both $|\mu|$ and $|\nabla\mu|$. Thus, even under extreme landmark-driven warping, regions outside the immediate deformation zones remain minimally distorted.

8.3. Hybrid Matching. Lastly, we tested our method in a synthetic experiment as well as a real-scenario application related to cortical surface registration. In the first test, the method was applied to a synthetic task requiring a diffeomorphic deformation that morphs an 'I'-shaped region on the sphere into a 'C' shape, while matching six pairs of corresponding landmarks and the entire image intensity. As shown in Fig.8b, the deformed image closely resembles the target image, landmarks are consistently matched and the obtained registration remains bijective.

Next, we tested our algorithm to register mean curvature and six sulci of two cortical surfaces. We used brain 32 as moving surface and brain 35 as template surface, and matched the six pairs of landmark curves meanwhile maximizing the correlation of their mean curvature. Fig.9 is the distribution of mean curvature on cortical surfaces, which shows that distribution of moving surface is more similar to that of fixed surface after deformation. Notably, after hybrid matching, the similarity in mean curvature distribution is significantly improved—from a pre-registration correlation coefficient of 0.083 to 0.581 post-registration (as opposed to just 0.123 when performing only landmark matching). We also compare the landmark matching effect of these two methods in Fig.10, and hybrid matching delivers both appropriate landmark registration and mean curvature alignment, enhancing the accuracy and anatomical interpretability of surface correspondence, which is an advantage in quantitative neuroimaging analysis and medical diagnosis.

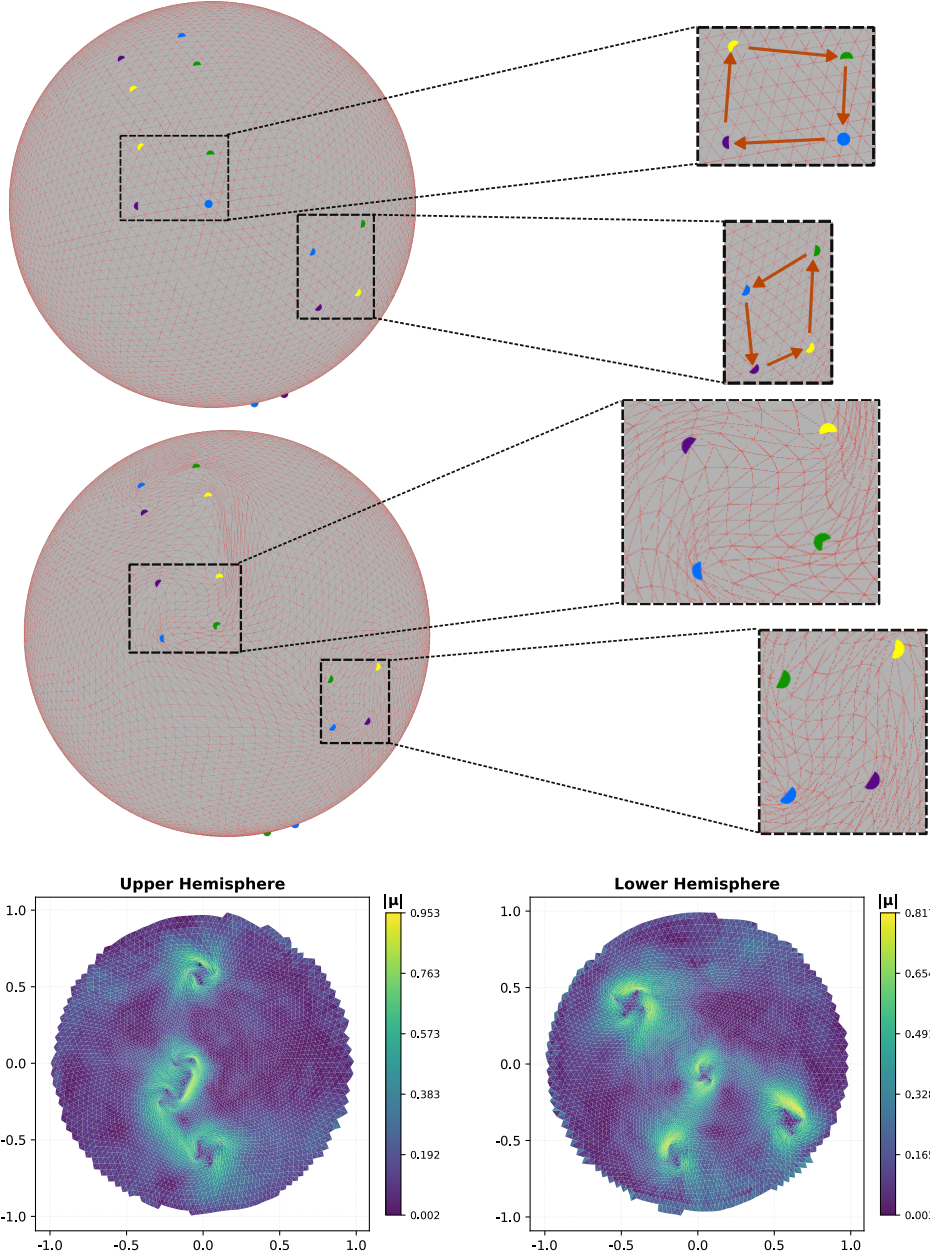
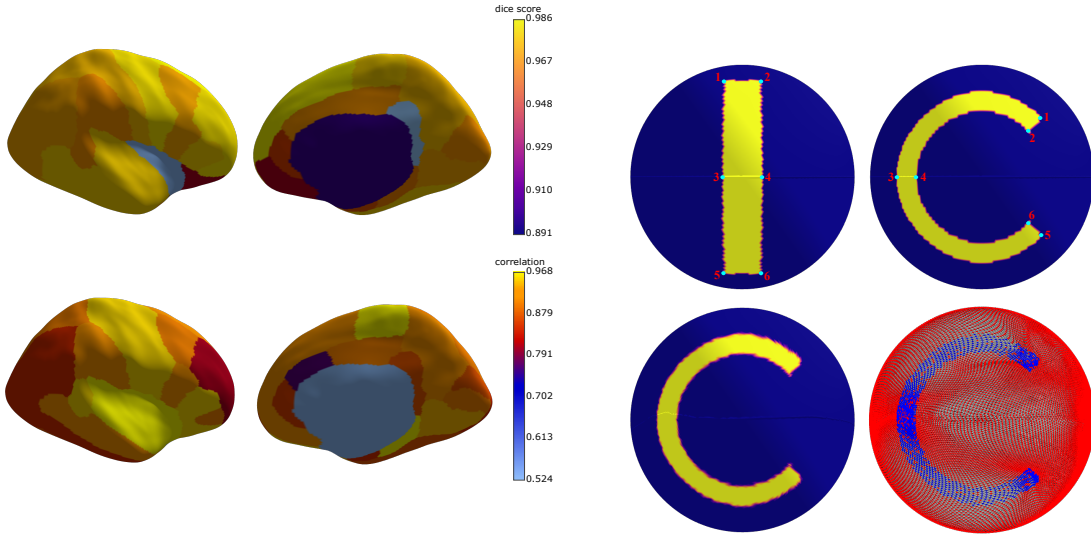


Figure 7: Results for the extreme distortion experiment 8.2. Top row: Landmarks to be matched, forming large-scale twists. Middle row: Deformation result of the surface after matching. Bottom row: Mapping results shown for both hemispheres, with color indicating the magnitude of the Beltrami coefficient.



(a) Sulci Depth and Parcellation Registration Result

(b) Synthetic Experiment of deforming an 'I' shape region on the sphere to the 'C' shape

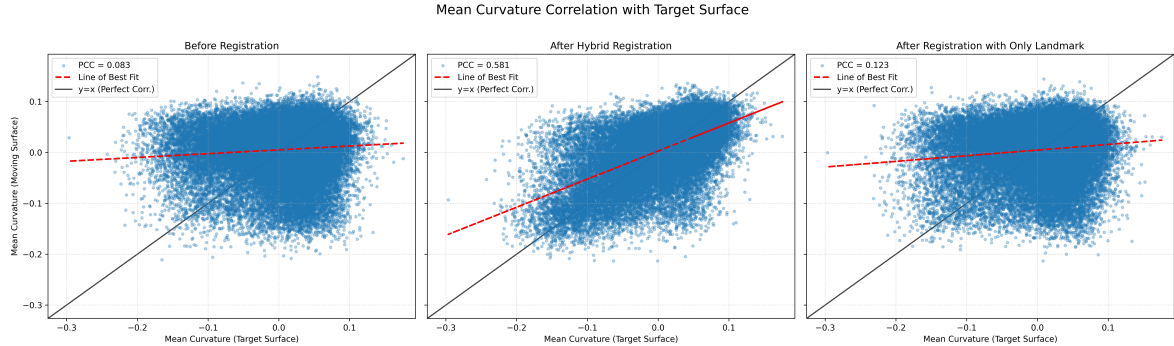


Figure 9: Mean curvature correlations between the moving surface and the target surface before and after registration. From left to right: (1) before deformation; (2) after hybrid matching registration; (3) after only-landmark matching registration. Alignment is visually and statistically improved after hybrid matching.

9. Discussion. In this paper we have introduced the concept Spherical Beltrami Differential, which has one to one correspondence with the equivalence class of spherical diffeomorphism up to the group of conformal mappings. Following this, we used Spherical Beltrami Network (SBN) to establish a neural optimization framework BOOST for spherical parameterization problems, which achieves optimization of spherical Beltrami differentials in a two-chart manner. Across multiple distinct testbeds including cortical surface alignment (Sec.8.1), extreme distortions (Sec.8.2), and hybrid intensity-landmark matching (Sec.8.3), BOOST matched or beat both classical numerical algorithms. Here, we try to analyze several potential factors that underlie

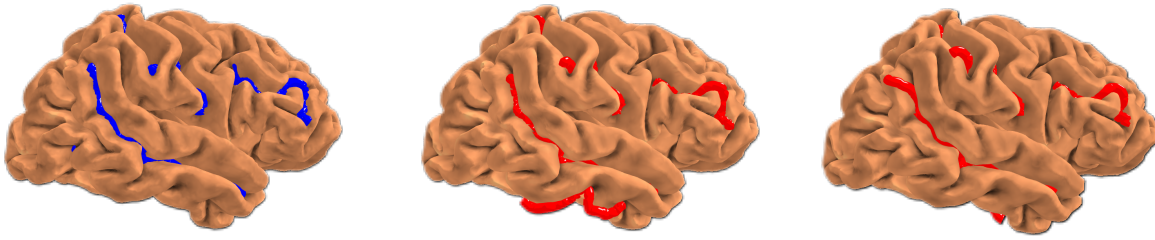


Figure 10: Comparing registration results: (left) fixed cortical surface, (center) deformed moving surface after hybrid matching, (right) deformed moving surface using landmark-only matching. Hybrid matching achieves both precise landmark alignment and improved mean curvature correlation.

this excellence:

1. **Power of SBN** BOOST’s effectiveness stems directly from the fidelity of LSQC’s neural surrogate, the Spectral Beltrami Network (SBN). By closely approximating the LSQC objective, SBN ensures that for any admissible Beltrami coefficient (BC) field, the predicted mapping tracks the true LSQC solution and usually remains diffeomorphic, thereby realizing the deformation prescribed by the input BC. This high-quality differentiable approximation gives BOOST a smooth, well-conditioned optimization landscape in Beltrami space, enabling gradient-based updates and suited for general spherical parameterization problems even some cases that explicit gradient on the deformation mapping is hard to compute.
2. **Free-boundary optimization** Traditional numerical algorithms usually impose hard boundary constraints and require mappings after each iteration to be non-overlapping, which shrinks the admissible solution space and increases the risk of getting trapped in sub-optimal local minima. SBN inherits the free-boundary perspective of LSQC energy, which provides a broader search space of mappings. Additionally, BOOST permits temporary foldings and boundary drift during optimization, which allows the optimizer bypass poor minima and folding would be removed when the folding loss dominates.
3. **Direct control on conformality** While classical methods often minimize angle distortion indirectly(e.g. Laplaic平滑) and deep learning approaches can control angle distortion only through penalizing the output mapping, our BOOST, by optimizing Beltrami coefficients directly via smoothness and magnitude penalties, achieves fine-grained angular-distortion control.

The excellence of SBN is not just that it “uses deep learning,” but that it faithfully encodes a mathematically well-behaved energy whose properties—existence, uniqueness, invariance, and resolution-independence, which translate directly into superior performance. By these, SBN achieves what neither classical solvers nor generic neural networks can: produce accurate surface mappings with well-controlled distortion and generalize across resolutions and different applications.

Though SBN represents a substantial advance and BOOST outperforms in applications, several pragmatic gaps remain:

1. **Not totally scale-free.** Currently, to handle ultra-high-resolution meshes, we in-

terpolate the solution from a lower-resolution “standard” grid, which is supported by the resolution-independence property of LSQC. However, this property is built on the assumption that beltrami coefficients on the three sub-triangles equal to that of the triangle before split. This condition might be inappropriate in high-curvature or feature-dense regions, and can introduce interpolation artifacts not faithfully reflecting fine-mesh geometry. An ideal remedy is a truly resolution-invariant architecture (e.g. continuous operators or adaptive patch hierarchies) that natively ingests Beltrami data and outputs deformation at arbitrary granularity, and that would be our future working direction.

2. **Limited to genus-0 topology.** Our current framework BOOST assumes genus-0 (spherical) topology. Extending to higher-genus or open surfaces is straightforward in principle—by redefining shape of parametrization domain as well as chart overlaps, and this is also left to future work.

10. Conclusions. In this work, we introduced a novel concept Spherical Beltrami Differential and build correspondence between Spherical Beltrami Differentials and spherical self-quasiconformal mappings. Following this, we proposed a two-chart optimization framework BOOST tailored to complex genus-0 surface mapping problems. As a key factor in BOOST, SBN can produce free-boundary quasiconformal mappings accurately following the input BCs. Besides, through designing three auxilliary losses \mathcal{L}_{bm} , \mathcal{L}_{bs} and $\mathcal{L}_{\text{folding}}$, BOOST resolves gluing issues between two hemispheres, and achieving smooth transitions across hemispherical boundaries. These capabilities establish BOOST as a robust and versatile framework for spherical parameterization problems. The excellence of BOOST has been demonstrated through extensive experiments and applications across three key categories: Landmark matching (Sec.8.1, 8.2), Intensity matching (e.g., Sec.8.1) and Hybrid matching (e.g., Sec.8.3).

In conclusion, it is the first time that we achieve optimization over surface Beltrami differentials and the outstanding performance of BOOST implies the potential of exploring optimization over surface Beltrami Differentials on general surfaces.

REFERENCES

- [1] A. BADEN, K. CRANE, AND M. KAZHDAN, *Möbius registration*, in Computer Graphics Forum, vol. 37, Wiley Online Library, 2018, pp. 211–220.
- [2] G. P. CHOI, A. GIRI, AND L. KUMAR, *Adaptive area-preserving parameterization of open and closed anatomical surfaces*, Computers in Biology and Medicine, 148 (2022), p. 105715.
- [3] G. P.-T. CHOI, K. T. HO, AND L. M. LUI, *Spherical conformal parameterization of genus-0 point clouds for meshing*, SIAM Journal on Imaging Sciences, 9 (2016), pp. 1582–1618.
- [4] P. T. CHOI, K. C. LAM, AND L. M. LUI, *Flash: Fast landmark aligned spherical harmonic parameterization for genus-0 closed brain surfaces*, SIAM Journal on Imaging Sciences, 8 (2015), pp. 67–94.
- [5] T. S. COHEN, M. GEIGER, J. KÖHLER, AND M. WELLING, *Spherical cnns*, arXiv preprint arXiv:1801.10130, (2018).
- [6] K. CRANE, U. PINKALL, AND P. SCHRÖDER, *Robust fairing via conformal curvature flow*, ACM Transactions on Graphics (TOG), 32 (2013), pp. 1–10.
- [7] C. ESTEVES, J.-J. SLOTINE, AND A. MAKADIA, *Scaling spherical cnns*, arXiv preprint arXiv:2306.05420, (2023).
- [8] B. FISCHL, *Freesurfer*, Neuroimage, 62 (2012), pp. 774–781.
- [9] X. GU, Y. WANG, T. F. CHAN, P. M. THOMPSON, AND S.-T. YAU, *Genus zero surface conformal*

mapping and its application to brain surface mapping, IEEE transactions on medical imaging, 23 (2004), pp. 949–958.

[10] X. GU AND S.-T. YAU, *Computing conformal structure of surfaces*, arXiv preprint cs/0212043, (2002).

[11] Y. GUO, Q. CHEN, G. P. CHOI, AND L. M. LUI, *Automatic landmark detection and registration of brain cortical surfaces via quasi-conformal geometry and convolutional neural networks*, Computers in Biology and Medicine, 163 (2023), p. 107185.

[12] R. HANOCKA, A. HERTZ, N. FISH, R. GIRYES, S. FLEISHMAN, AND D. COHEN-OR, *Meshcnn: a network with an edge*, ACM Transactions on Graphics (ToG), 38 (2019), pp. 1–12.

[13] M. ISENBURG, S. GUMHOLD, AND C. GOTSMAN, *Connectivity shapes*, in Proceedings Visualization, 2001. VIS'01., IEEE, 2001, pp. 135–152.

[14] M. JIN, J. KIM, F. LUO, AND X. GU, *Discrete surface ricci flow*, IEEE Transactions on Visualization and Computer Graphics, 14 (2008), pp. 1030–1043.

[15] L. KHAREVYCH, B. SPRINGBORN, AND P. SCHRÖDER, *Discrete conformal mappings via circle patterns*, ACM Transactions on Graphics (TOG), 25 (2006), pp. 412–438.

[16] K. H. LAI AND L. M. LUI, *Point cloud surface parametrization with hand and leg: Hausdorff approximation from node-wise distances and localized energy for geometry*, arXiv preprint arXiv:2501.13737, (2025).

[17] R. LAI, Z. WEN, W. YIN, X. GU, AND L. M. LUI, *Folding-free global conformal mapping for genus-0 surfaces by harmonic energy minimization*, Journal of Scientific Computing, 58 (2014), pp. 705–725.

[18] K. C. LAM AND L. M. LUI, *Landmark-and intensity-based registration with large deformations via quasi-conformal maps*, SIAM Journal on Imaging Sciences, 7 (2014), pp. 2364–2392.

[19] P. J. LAMONTAGNE, T. L. BENZINGER, J. C. MORRIS, S. KEEFE, R. HORNBECK, C. XIONG, E. GRANT, J. HASSENSTAB, K. MOULDER, A. G. VLASSENKO, ET AL., *Oasis-3: longitudinal neuroimaging, clinical, and cognitive dataset for normal aging and alzheimer disease*, medrxiv, (2019), pp. 2019–12.

[20] B. LÉVY, S. PETITJEAN, N. RAY, AND J. MAILLOT, *Least squares conformal maps for automatic texture atlas generation*, ACM Transactions on Graphics, 21 (2002), pp. 10–p.

[21] L. LIEBEL AND M. KÖRNER, *Auxiliary tasks in multi-task learning*, arXiv preprint arXiv:1805.06334, (2018).

[22] L. M. LUI, K. C. LAM, S.-T. YAU, AND X. GU, *Teichmuller mapping (t-map) and its applications to landmark matching registration*, SIAM Journal on Imaging Sciences, 7 (2014), pp. 391–426.

[23] L. M. LUI AND T. C. NG, *A splitting method for diffeomorphism optimization problem using beltrami coefficients*, Journal of Scientific Computing, 63 (2015), pp. 573–611.

[24] L. M. LUI, S. THIRUVENKADAM, Y. WANG, P. M. THOMPSON, AND T. F. CHAN, *Optimized conformal surface registration with shape-based landmark matching*, SIAM Journal on Imaging Sciences, 3 (2010), pp. 52–78.

[25] L. M. LUI, Y. WANG, T. F. CHAN, AND P. THOMPSON, *Landmark constrained genus zero surface conformal mapping and its application to brain mapping research*, Applied Numerical Mathematics, 57 (2007), pp. 847–858.

[26] L. M. LUI, T. W. WONG, W. ZENG, X. GU, P. M. THOMPSON, T. F. CHAN, AND S.-T. YAU, *Optimization of surface registrations using beltrami holomorphic flow*, Journal of scientific computing, 50 (2012), pp. 557–585.

[27] Z. LYU, L. M. LUI, AND G. P. CHOI, *Spherical density-equalizing map for genus-0 closed surfaces*, SIAM Journal on Imaging Sciences, 17 (2024), pp. 2110–2141.

[28] F. MILANO, A. LOQUERCIO, A. ROSINOL, D. SCARAMUZZA, AND L. CARLONE, *Primal-dual mesh convolutional neural networks*, Advances in Neural Information Processing Systems, 33 (2020), pp. 952–963.

[29] D. QIU, K.-C. LAM, AND L.-M. LUI, *Computing quasi-conformal folds*, SIAM Journal on Imaging Sciences, 12 (2019), pp. 1392–1424.

[30] J. REN, N. AN, Y. ZHANG, D. WANG, Z. SUN, C. LIN, W. CUI, W. WANG, Y. ZHOU, W. ZHANG, ET AL., *Sugar: Spherical ultrafast graph attention framework for cortical surface registration*, Medical Image Analysis, 94 (2024), p. 103122.

[31] Z. XU AND L. M. LUI, *A neural optimization framework for free-boundary diffeomorphic mapping problems and its applications*, arXiv preprint arXiv:2511.11679, (2025).

[32] F. ZHAO, Z. WU, L. WANG, W. LIN, AND G. LI, *Fast spherical mapping of cortical surface meshes using deep unsupervised learning*, in International Conference on Medical Image Computing and

Computer-Assisted Intervention, Springer, 2022, pp. 163–173.

[33] F. ZHAO, S. XIA, Z. WU, D. DUAN, L. WANG, W. LIN, J. H. GILMORE, D. SHEN, AND G. LI, *Spherical u-net on cortical surfaces: methods and applications*, in Information Processing in Medical Imaging: 26th International Conference, IPMI 2019, Hong Kong, China, June 2–7, 2019, Proceedings 26, Springer, 2019, pp. 855–866.